mechanisms of impulsive pressures, and such a digression may shift the focus of our argument. Therefore, we will concentrate on the behavior of a spherical cavitation bubble in an US field and the resulting shock wave phenomenon against the cell.

Cavitation bubble behavior depends on the properties of the surrounding boundaries[40][41]. The critical relative distance affecting the cavitation bubble behavior is defined as L/R_{max}, where L is the distance between the boundary and the bubble inception position and R_{max} is the maximum bubble expansion radius. When NBs are distributed uniformly in the medium and each NB produces a single cavitation bubble at $L/R_{max} > 4$ [42], the bubble motion can be analyzed spherically.

Bubble dynamics

We assume that the US contrast agents are destroyed by US and the internal gas C_3F_8 is trapped in the crevices of the debris of the destroyed agents; additionally, the cavitation bubbles are assumed to be generated from the gas trapped in the crevices. Furthermore, we consider the gas as cavitation nuclei, as modeled by Harvey *et al.* [19]. We assume that spherical cavitation bubbles with a nanometer diameter size can be analyzed as a continuum. The motion of a free spherical cavitation bubble is given by the Keller-Miksis equation [43] as shown below. This equation is corrected to the first order of the Mach number of the bubble wall motion. The error term is the order $\left(\dot{R}/C_L\right)^2$ [44].

$$\ddot{R}\left(1-\frac{1}{C_L}\dot{R}\right)+\frac{3}{2}\dot{R}^2\left(1-\frac{1}{3C_L}\dot{R}\right)=\left(1+\frac{\dot{R}}{C_L}\right)\frac{1}{\rho_L}\left[P_{r=R}(t)-P_C\left(t+\frac{R}{C_L}\right)-P_0\right]+\frac{R}{\rho_L C_L}\frac{dP_{r=R}(t)}{dt} \tag{1}$$

the pressure $P_{r=R}$ at the bubble surface is given by the equation:

$$P_{r=R}(t)=\left(P_0+\frac{2\sigma_L}{R_0}\right)\left(\frac{R_0}{R}\right)^{3r}-\frac{2\sigma_L}{R}-\frac{4\mu_L}{R}\dot{R} \tag{2}$$

the oscillation pressure P_C is given by the equation:

$$P_C(t)=\left|P_A\right|\sin\omega t \tag{3}$$

where R is the radius of the bubble; C_L, sound velocity in liquid (1497 m/s); ρ_L, density of water (997 kg/m^3); P_0, atmospheric pressure (101.3 kPa); R_0, the initial bubble radius; γ, adiabatic exponent of a gas (1.07) [45]; μ_L, the liquid shear viscosity (0.89 mPa·s); σ_L, surface tension of water (72 mN/m); P_A, peak positive pressure measured in the experiments; and ω, the circular frequency. Thermal diffusion at the bubble wall and noncondensable gas were ignored.

When a cavitation bubble collapses, a spherical shock wave is emitted as the bubble rebounds. The shock wave interacts with the surrounding cells, resulting in cell membrane damage. The distance of the shock wave propagation from the center of the bubble r_C required to damage to the cell membrane is given by the equation [46]:

$$r_C \approx \frac{P_{max}R_{min}}{\varepsilon_C \rho_L C_L^2} \tag{4}$$

where P_{max} is the maximum pressure when the bubble reaches the minimum radius R_{min} and ε_C is the static critical strain required to damage the membrane. ε_C is estimated to be 0.02–0.03 for the red blood cell membrane [47].

The shock wave pressure Ps, defined as the peak value of the shock wave pressure, decreases as approximately $1/r_S$ while it propagates outward [48]; thus, Ps is given by the equation:

$$P_S = \frac{P_{max} R_{min}}{r_S} \tag{5}$$

where r_S is the radial distance of the shock front from the origin.

The acoustic energy Es of a spherical shock wave is given by the equation [49]:

$$E_S = \frac{4\pi r_S^2}{\rho_L C_L} \int_0^{t'} P(t)^2 dt \tag{6}$$

By assuming that the shock wave has wave characteristics that vary in the form of exponential decay with respect to time, we defined the pressure profile P(t) as follows:

$$P(t) \cong P_s \exp\left[\frac{-t \cdot \ln 2}{t_S}\right] \tag{7}$$

where Ps is the peak pressure and t_S is the full width at half-maximum (FWHM) pulse duration of a shock wave (i.e., the time satisfying the condition $(P_S + P_0)/2$), which is numerically obtained. From eqn (6), Es is given as follows [50]:

$$E_S = \frac{2\pi R_{min}^2 P_{max}^2 t_s}{\rho_C C_L \ln 2} \tag{8}$$

On the assumption that Es is conserved during the shock wave propagation, t_{rC} at $r = r_C$ is described as follows:

$$t_{r_c} = \frac{\rho_L C_L \ln 2 E_S}{2\pi r_C^2 P_{max}^2} \tag{9}$$

The shock wave impulse I at $r = r_C$ is given as follows:

$$I_{r_c} = \frac{\rho_L C_L E_S}{2\pi r_C R_{min} P_{max}} \tag{10}$$

The equ (1) was calculated up to 50 periodic times using a fourth-order Runge-Kutta method to determine the maximum pressure P_{max}, maximum bubble radius R_{max}, and minimum bubble radius R_{min}, respectively. The chaotic behavior of the bubble motion due to the nonlinear oscillation was not considered.

2.3. Molecular dynamics simulation

Modeling of lipid bilayer

The cell membrane is a thin film (approximately 5 nm) composed of lipids and proteins. The lipid bilayer forms the basic structure of the membrane, while the protein molecules exist as dissolved entities in this layer. Four major phospholipids predominate in the plasma membrane of many mammalian cells: phosphatidylcholine (DPPC), sphingomyelin, phosphatidylserine, and phosphatidylethanolamine [51]. Following the study of Koshiyama

et al. [31], we calculated the interaction of a single lipid bilayer with a shock wave. The lipid bilayer was designed as a 32 DPPC lipid bilayer sandwiched between 2 layers of 2400 water molecules in a rectangular calculation box. The long axis (z axis) of the rectangular box was perpendicular to the bilayer plane (xy plane). The water molecules were calculated using a simple point charge (SPC) model, and all the bond interactions between the atoms in the DPPC molecules were calculated. The stable liquid-crystal phase bilayer was calculated for several tens of nanoseconds under a constant temperature of 50°C and a pressure of 101.3 kPa with periodic boundary conditions.

Shock wave impulse

The shock wave impulse per unit area I is defined as follows [30]:

$$I = \int_0^{t_+} p(t)dt \tag{11}$$

where t is the time; $p(t)$, the pressure near the cells in water; and t_+, the positive phase duration of a half cycle of the shock wave [30]. On the basis of the definition of impulse, the shock impulse I can be regarded as the increment in the momentum of water divided by an area A (the cross-sectional area normal to the z direction of the simulation box) on which the pressure $p(t)$ is exerted. The shock wave impulse is given as follows:

$$I = \frac{M(t_+) - M(0)}{A} \tag{12}$$

where $M(t)$ is the momentum of water at time t. At time $t = 0$, the shock wave did not reach the cells, and the water molecules in the front of the shock wave were at rest; therefore, $M(0) = 0$. When $t = t_+$, the shock wave passed over a small volume of water near the cells, and the momentum $M(t_+) = I \times A$ was transferred to the small volume of water. At the beginning of shock wave simulation, the momentum $M(t_+)$ was applied to water molecules adjacent to the bilayer in a volume $A \times L_Z$, where $A = 3.77$ nm $\times$ 2.72 nm = 10.25 nm^2 and L_Z is the length of the volume of water in the z direction [31]. The choice of L_Z is arbitrary, and we set $L_Z = 4$ nm, which is almost equal to the initial thickness of the bilayer. This is because the present simulation was focused on the behavior of the bilayer with the excess momentum $M(t_+)$ added by the shock wave. The change in the momentum of the water molecules at the beginning of the shock simulation was numerically implemented by the addition of an average velocity V to the thermal velocity of the water molecules in the equilibrated bilayer/water system.

The average velocity V is given by

$$V = \frac{M(t_+)}{mN} = \frac{I \times A}{mN} \tag{13}$$

where m is the weight of a water molecule and N (~1000) is the number of water molecules in the volume $A \times L_Z$. The impulse I is increased from 0 to 100 mPa·s at an interval of 2.5 mPa·s, and V is then changed from 0 to 25600 m/s. The average velocity V corresponds neither to the speed of sound in water nor to the propagation speed of the shock wave. It represents only the increase in the momentum of water molecules due to the shock wave. The modeling of the shock wave by the impulse enables qualitative comparison between the present numerical results and the previous experimental ones.

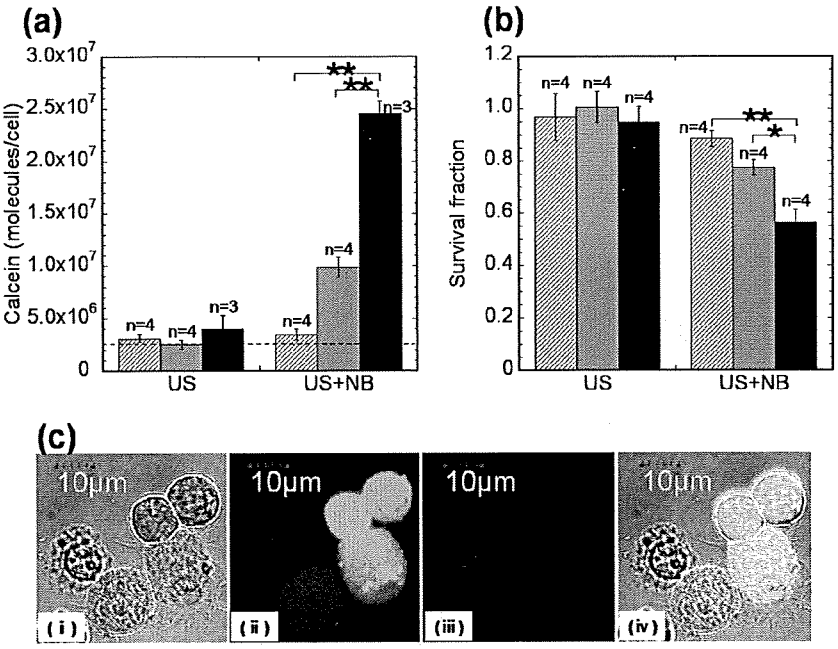

Fig. 3 Effects of NBs on the uptake of calcein (molecular weight: 622). 293T cells with and without NBs were exposed to US with varying US pressure P_A (0.2, 0.3, and 0.5 MPa). Duty ratio, 50%; number of pulses, 2000; pulse repletion frequency (PRF), 250 Hz; and exposure time, 10 s. (a) The number of intracellular molecules per cell. The calcein uptake of the control samples that are without US +NB is indicated as the broken, which is similar to that of US alone. Values are expressed as means ± S.E.M. (n = 3-4), where n is the number of samples. Statistical analysis for the calcein uptake was performed by Kruskal-Wallis test. When the Kruskal-Wallis test was significant, the differences between each group were estimated using the Scheff's F test as a post-hoc procedure. The differences were considered to be significant at $P < 0.01$(**). (b) Survival fractions determined by the MTT assay. Values are expressed as means ± S.E.M. (n = 4). Statistical analysis was performed by Bartlett test followed by one-way analysis of variance (ANOVA). When the one-way ANOVA was significant, the differences between each group were estimated using the Tukey-Kramer test as a post-hoc procedure. The differences were considered to be significant at $P < 0.05$ (*) or $P < 0.01$(**). ▨ : 0.2 MPa, ▩ : 0.3 MPa, ■ : 0.5 MPa. (c) Confocal fluorescence microscopy showing (i) differential interference contrast, (ii) fluorescence images, (iii) representative viable 293T cells exposed to US in the presence of NBs and (iv) color-merged image. In fluorescence staining, PI was used to confirm that the cells showing calcein uptake were viable. Scale bars = 10 μm. US pressure was 0.5 MPa; duty ratio, 50%; number of pulses, 2000; pulse repletion frequency (PRF), 250 Hz; and exposure time, 10 s.

3. Results and Discussion

Observation of cavitation bubbles

First, we investigated the number of calcein molecules delivered into cells in the presence of NBs and US in the experimental system as seen in Fig. 2. The medium containing NBs was a white emulsified suspension. After exposure to US, the medium became transparent, and fragmented debris was found floating on the surface. Atomized particles were detected on the surface with increasing US pressure. In contrast, these particles were not observed with increasing US pressure in the absence of NBs. This phenomenon indicates that impurities in the medium enhance the generation of cavitation bubbles, resulting in the production of capillary waves and subsequent atomized particles [26]. The mean diameter d of the atomized particles due to capillary waves generated by US on the free surface is determined by the liquid surface tension σ_L, liquid density ρ_L, and US frequency f, which is given by eqn (A1). Thus, the mean diameter of the atomized particles is calculated to be 7.9 μm for 1-MHz US. The detailed mechanism of atomized particle generation has been reported by Yule and Al-Suleimani [52].

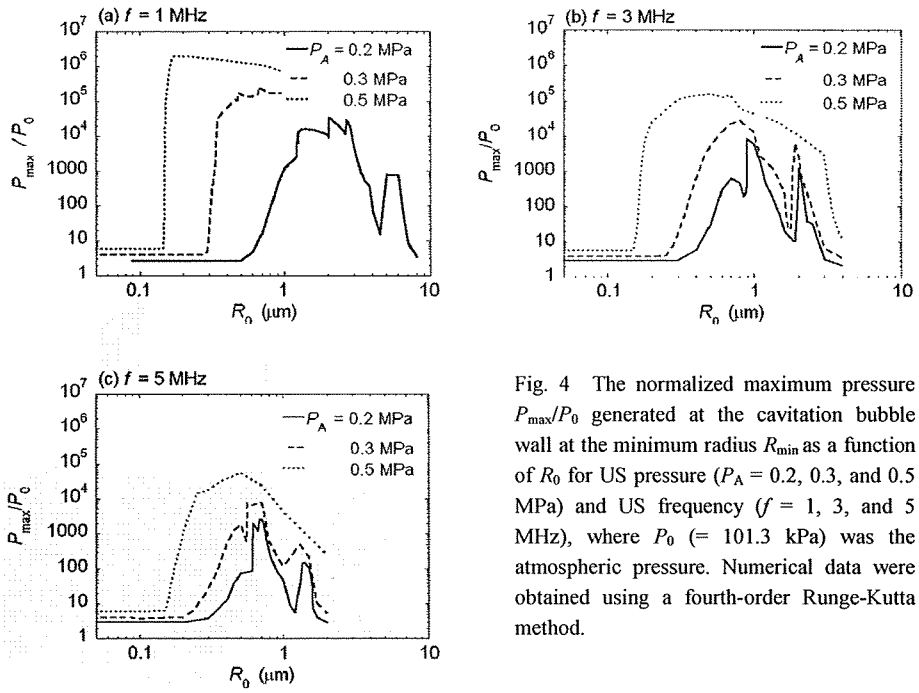

Fig. 4 The normalized maximum pressure P_{max}/P_0 generated at the cavitation bubble wall at the minimum radius R_{min} as a function of R_0 for US pressure (P_A = 0.2, 0.3, and 0.5 MPa) and US frequency (f = 1, 3, and 5 MHz), where P_0 (= 101.3 kPa) was the atmospheric pressure. Numerical data were obtained using a fourth-order Runge-Kutta method.

Uptake of calcein into cells by sonoporation

Figure 3a shows the number of calcein molecules per cell with varying US pressure in the presence/absence of NBs. The duration of exposure to US was 10 s. The calcein uptake of the control samples that are without US +NB is indicated as the broken, which is similar to that of US alone. The presence of the NBs caused a significant increase in the calcein uptake with increasing US pressure, resulting in the delivery of 2.5×10^7 calcein molecules per cell at P_A = 0.5 MPa ($P < 0.01$). The increase in the uptake was associated with the increase in the generation of the atomized particles.

Figure 3b shows the survival fraction of cells exposed to US with and without NBs measured by the MTT assay. US alone did not affect the survival fraction at these pressure values [26]; however, the survival fraction in the presence of NBs decreased with increasing pressure ($P < 0.01$). The uptake of exogenous molecules was inversely proportional to the survival fraction; this finding was in agreement with previous results [26][53]. To confirm that the calcein molecules actually entered the cytoplasm, confocal fluorescence microscopy was performed. Figure 3c shows (i) the differential interference contrast, (ii) fluorescence images, and (iii) representative viable 293T cells exposed to US (0.5 MPa) in the presence of NBs and (iv) color-merged image. In some fluorescence staining, PI was used to confirm that the cells showing calcein uptake were viable and excluded PI (Fig. 3c(iii)). Some cells treated with US in the presence of NB showed intense fluorescence that was uniformly distributed throughout the entire cell.

Motion of cavitation bubbles in the field of ultrasound

From the experimental results, we assumed that cavitation bubbles were related to the transient membrane permeability and subsequent molecular uptake into cells. Next, we analyzed the behavior of a single spherical cavitation bubble in a wide range of parameters including the experimental conditions. Figure 4 shows the relationship between the normalized maximum pressure P_{max}/P_0 generated on the surface of the cavitation bubble wall at the minimum radius R_{min}, and the bubble initial radius R_0, where the atmospheric pressure P_0 was 101.3 kPa. R_0 was varied from 0.05 to 10 μm, US frequency f was 1, 3, and 5 MHz, and the US pressure P_A 0.2, 0.3 and 0.5 MPa. Figure 4a is when f = 1 MHz. The

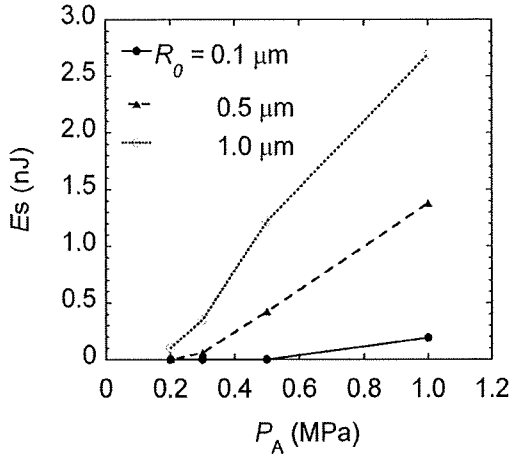

Fig. 5 Relationship between the shock wave energy *Es* given by eqn (8) and the US pressure P_A. The US frequency f was 1 MHz. Numerical data were obtained using a fourth-order Runge-Kutta method.

P_{max}/P_0 increased gradually with increasing R_0, and a peak was obtained at around R_0 = 1.2~3.0 μm. After the first peak, P_{max}/P_0 decreased rapidly, and the second peak was obtained at around R_0 = 5~6 μm. These irregularities are due to the nonlinear cavitation bubble motion. The peak P_{max}/P_0 increased with increasing P_A, and its position shifted to lower values of R_0. When R_0 = 0.635 μm (= 1.27 ÷ 2 μm) that is the initial radius of NBs used in the experiment, P_{max}/P_0 = 4.9 → 1.3 × 10^6 when P_A= 0.2 → 0.5 MPa. In Fig. 3a, the uptake of calcein increases by a factor of 3.6 when P_A= 0.2 → 0.5 MPa. Thus, the increase in P_{max}/P_0 related to the increase in the uptake, indicating that shock waves generated by cavitation bubbles were involved in the uptake of calcein.

Figures 4b and 4c shows the profile of P_{max}/P_0 when f = 3, and 5MHz, respectively. The P_{max}/P_0 decreased when f = 1 → 5 MHz, i.e. the generation of cavitation bubbles is suppressed with increasing US frequency. The fact that the threshold of generation of cavitation bubbles decreases with increasing frequency is in agreement with theoretical [54] and recent experimental results obtained by broadband noise [23]. However, it should be noted that the pressure values were overestimated outside the range of values used for deriving equations.

Interaction of cell membrane with shock wave emitted from a cavitation bubble

When a cavitation bubble reaches its minimum radius R_{min}, it expands and moves the surrounding liquid in the radial direction, thereby resulting in a pressure wave in the vicinity of the bubble wall. The wave propagates outward with a steep pressure front to become a shock wave.

Figure 5 shows the relationship between the shock wave energy *Es* given by eqn (8) and the US pressure P_A at the US frequency f of 1 MHz. The initial bubble radius R_0 varied from 0.1 to 1.0 μm. E_S increased with increasing P_A and R_0, where *Es* was 2.7 nJ at P_A = 1 MPa and R_0 = 1.0 μm.

The shock wave attenuates approximately proportional to $1/r_S$ (r_S: the radial distance of the shock front from the origin) [48][55][56] and interacts with the surrounding cells, resulting in cell membrane damage. In addition, a rapid bubble radial expansion mechanically damages the surrounding cells. Figure 6 shows the shock wave propagation distances (r_C) from the point of its generation as a function of the initial bubble radius R_0 at the US frequency f of 1 MHz, where R_{max} is the calculated maximum bubble radius, and ε_C is necessary to disrupt the membrane. Evans *et al.* [47] reported that ε_C was estimated to be 0.02–0.03 for the red blood cell membrane. In Fig. 6, the shock wave can cause membrane damage at distances less than r_C. The relationship of $r_C > R_{max}$ was satisfied for all values of P_A considered in the present study, i.e., the shock wave was regarded as the main factor of membrane damage rather than bubble expansion. From eqn (A2), the characteristic radius r_0 for a single lipid

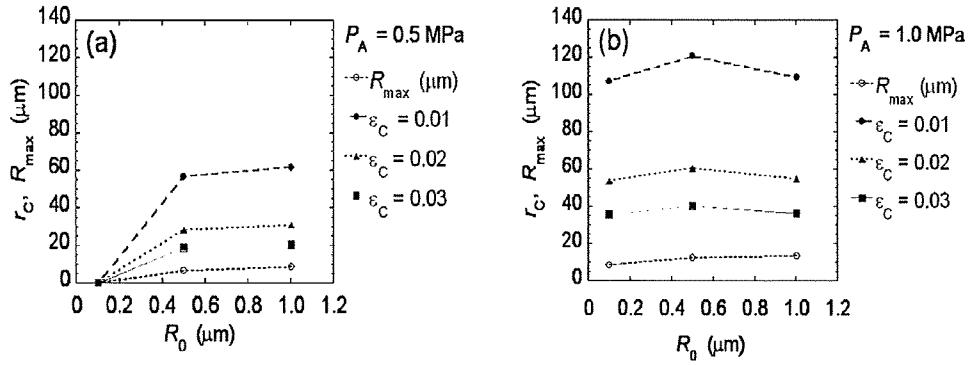

Fig. 6 Potential radius r_C of inducing cell damage by a shock wave from a cavitation bubble and the maximum bubble expansion radius R_{max}, where r_C was given by eqn (4). The initial bubble radius R_0 was 0.1–1.0 μm. The critical strain ε_C was 0.01– 0.03. The US pressure P_A was 0.5–1.0 MPa. The US frequency f was 1 MHz. Numerical data were obtained using a fourth-order Runge-Kutta method.

bubble was calculated to be 19 μm prior to the US exposure. If a single NB produces multiple cavitation bubbles, the conditions $r_C > r_0$ and $r_C > R_{max}$ are satisfied, i.e., the entire area of the medium can be regarded as the shock wave dominant area; therefore, all cells in the medium would be loaded by the shock waves created by the cavitation bubbles.

Figure 7 shows the relationship between P_A and the impulse Ir_c at r_C with varying ε_C, given by eqn (10) at the US frequency f of 1 MHz. When R_0 = 0.5 μm (Fig. 7a), a peak of each characteristic line was obtained at P_A = 0.3 MPa, and the value increased with increasing ε_C. The peak was due to the bubble natural frequency. When R_0 = 1.0 μm (Fig. 7b), peaks were not observed in the figure; however, the lines decreased rapidly with increasing P_A to reach a constant value. This figure indicates that a spherical cavitation bubble with a radius of 0.5–1.0 μm generates impulse values up to 100 mPa·s.

MD simulation of water molecular delivery into the lipid bilayer with shock wave impulse

It is desirable to calculate the number of calcein molecules delivered into cells with MD simulation for comparison with the experimental results. However, to our knowledge, there are no reliable calculation parameters such as force fields or partial charges to reproduce calcein thermodynamic properties and quantum factors. In the present study, we compared the number of water molecules delivered into the lipid bilayer calculated by MD simulation with that of calcein molecules obtained experimentally.

Figure 8 shows the relationship between the shock wave impulse and the penetration rate of water molecules into the bilayer obtained by MD simulation. The penetration ratio of water molecules into the lipid bilayer increased with increasing shock wave impulse. Water molecules were delivered into the cells at the rate of 0–0.3 molecules/(ps·nm^2) at I = 0–11 mPa·s at R_0 = 0.5 μm and ε_C = 0.03 (Figs. 7a and 8). In contrast, at R_0 = 1.0 μm and ε_C = 0.03 (Figs. 7b and 8), water molecules were delivered into the cells at a rate of 0.2–7.6 molecules/(ps·nm^2) at I = 7.2–95 mPa·s.

Although it is reported that water molecules can penetrate into the cytoplasm across the membrane on macroscopic time scales [51], the event rarely occurs on molecular time scales (below nanosecond time scales). However, in the present molecular simulation, water penetration was observed on picosecond time scales. Here, we assumed that at the cell radius r of 5 μm, the shock wave impulse was loaded to a cell from above, and the duration of the impulse was 1 ps. The surface area of the cell hemisphere was given by $2\pi r^2$, and the number of water molecules delivered into the lipid bilayer was calculated to be around 10^7~10^9. The radius of the water molecule was approximately 0.1 nm, and the radius of calcein was estimated to be 0.68 nm [30]. Although the size of the calcein molecule was

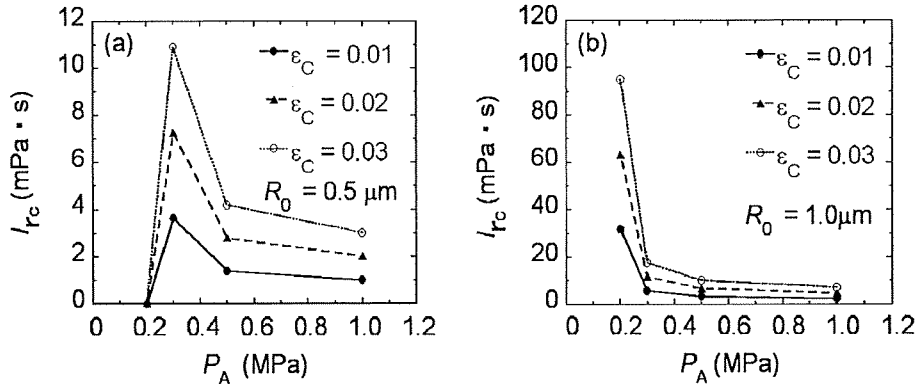

Fig. 7 Relationship between the shock wave impulse I_{rC} (mPa·s) and the US pressure P_A (0.2–1.0 MPa). The US frequency f was 1 MHz. The critical strain ε_C was 0.01–0.03. (a) R_0 = 0.5 μm, (b) R_0 = 1.0 μm. Numerical data were obtained using a fourth-order Runge-Kutta method.

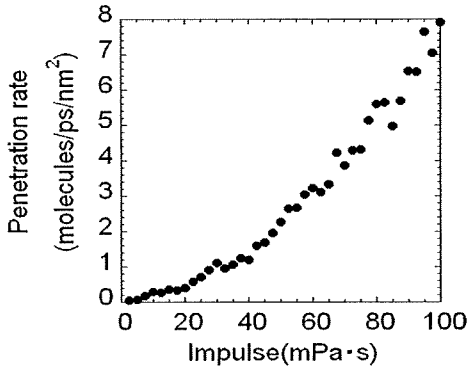

Fig. 8 Relationship between the shock wave impulse and the penetration ratio of water molecules calculated by MD simulation, in which the penetration ratio was calculated in the hydrophobic region at the instant of termination of simulation divided by the cross-sectional area (A = 10.25 nm^2) and the simulation time.

larger than that of the water molecule by a factor of 6.8, the number of delivered calcein molecules in the order of 10^7 per cell (Fig. 3) corresponded to the numerical values. We should note that the estimation of calcein delivery is on experimental time scales (several seconds have elapsed after exposure to ultrasound). On these time scales, the number of delivered water molecules might become considerably larger than that of calcein molecules because many shock waves are generated by pulsating bubbles' impact on membranes. At present, we have investigated water pore formation in lipid bilayers induced by the shock wave impulse [33]. This study suggests that more water penetration induces more larger structural changes in the lipid bilayer. Although it is not possible to estimate the number of water molecules that penetrate into the cells after induction by shock waves by using any other method, the results of the experimental estimation of calcein and numerical estimation of water molecules in the present study imply that the penetration of a large number of water molecules is required before the entry of large molecules. Because water penetration depends on the shock wave impulse generated in the conditions studied here, we believe that the impulse of the shock waves generated by the cavitation bubbles is one of the important parameters for permeabilization during sonoporation.

4. Conclusion

In the present study, experimental, theoretical and numerical analyses were performed to investigate cavitation bubbles mediated molecular delivery during sonoporation. The following conclusions were obtained.

1. Experimental observation using lipid nano/microbubbles indicated that increasing US

pressure increased uptake of fluorescent molecules, calcein, into 293T human, and decreased survival fraction.

2. Theoretical analysis based on a spherical gas bubble dynamics indicated that the impulse of the shock wave (i.e., the pressure integrated over time) generated by the collapse of a cavitation bubble created by nano/microbubbles was one of dominant factors for exogenous molecules to enter into the cell membrane rather than bubble expansion.

3. Molecular dynamics simulation revealed that the number of exogenous molecules delivered into the cell membrane increased with increasing the shock wave impulse.

4. The impulse of the shock wave generated by cavitation bubbles was one of important parameters for causing exogenous molecular uptake into living cells during sonoporation.

Acknowledgments

TK acknowledges the Grant-in-Aid for Scientific Research (B) (20300173); the Grants-in-Aid for Scientific Research on Priority Area, MEXT (20015005); and the Grant for Research on Advanced Medical Technology, the Ministry of Health, Labour and Welfare of Japan (H19-nano-010). YT acknowledges the Grant-in-Aid for Scientific Research (C) (20560144), and KK acknowledges the Grant-in-Aid for Young Scientists (B) (20760114—0004).

Appendix

Atomized liquid particles generated with US

The mean diameter d of the atomized particles due to capillary waves generated by US on the free surface is given by the equation [57]:

$$d \cong 1.9\left[\frac{\sigma_L}{\rho_L f^2}\right]^{\frac{1}{3}} \tag{A1}$$

where f is the acoustic frequency (varied from 20 kHz to 3 MHz); ρ_L, the liquid density (997 kg/m^3 for water at 25°C); and σ_L, the liquid surface tension of 72 mN/m. Thus, the mean diameter of the atomized particles was calculated to be 7.9 μm for 1 MHz US. The detailed mechanism of atomized particle generation has been reported by Yule and Al-Suleimani [52].

Characteristic radius r_0 occupied by a single bubble

In the abovementioned calcein experiment, 110 μL of a medium that contained 10% NBs was irradiated by US. The maximum geometrical characteristic radius r_0 occupied uniformly by a single NB is given as follows:

$$r_0 = \left(\frac{3Ah}{4\pi N_0}\right)^{\frac{1}{3}} \tag{A2}$$

where A is the area of the base of a well in the 48-well plate; h, height of the medium; N_0, the number of US contrast agents. For micelle bubbles, r_0 was calculated to be 19 μm at $N_0 = 3.4 \times 10^8$ bubbles/mL.

References

(1) H. Zhegn, O. Mukdadi, R. Shandas, Theoretical predictions of harmonic generation from submicron ultrasound contrast agents for nonlinear biomedical ultrasound imaging. *Physics in Medicine and Biology*, Vol.51, No.3 (2006), pp.557-573.

(2) W. Hayduk, H. Laudie, Prediction of diffusion-coefficients for nonelectrolytes in dilute

aqueous-solutions. *Aiche Journal*, Vol.20, No.3 (1974), pp.611-615.

(3) A. Kabalnov, D. Klein, T. Pelura, E. Schutt, J. Weers, Dissolution of multicomponent microbubbles in the bloodstream: 1. Theory. *Ultrasound in Medicine and Biology*, Vol.24, No.5 (1998), pp.739-749.

(4) E.C. Unger, T. Porter, W. Culp, R. Labell, T. Matsunaga, R. Zutshi, Therapeutic applications of lipid-coated microbubbles. *Advanced Drug Delivery Reviews*, Vol.56, No.9 (2004), pp.1291-1314.

(5) J.R. Lindner, Microbubbles in medical imaging: current applications and future directions. *Nature Reviews Drug Discovery*, Vol.3, No.6 (2004), pp.527-532.

(6) R. Bekeredjian, S. Chen, P.A. Frenkel, P.A. Grayburn, R.V. Shohet, Ultrasound-targeted microbubble destruction can repeatedly direct highly specific plasmid expression to the heart. *Circulation*, Vol.108, No.8 (2003), pp.1022-1026.

(7) T.R. Porter, P.L. Iversen, S. Li, F. Xie, Interaction of diagnostic ultrasound with synthetic oligonucleotide-labeled perfluorocarbon-exposed sonicated dextrose albumin microbubbles. *Journal of Ultrasound in Medicine*, Vol.15, No.8 (1996), pp.577-584.

(8) S.M. Stieger, C.F. Caskey, R.H. Adamson, S. Qin, F.R. Curry, E.R. Wisner, K.W. Ferrara, Enhancement of vascular permeability with low-frequency contrast-enhanced ultrasound in the chorioallantoic membrane model. *Radiology*, Vol.243, No.1 (2007), pp.112-121.

(9) A.Y. Ammi, R.O. Cleveland, J. Mamou, G.I. Wang, S.L. Bridal, W.D. O'Brien, Ultrasonic contrast agent shell rupture detected by inertial cavitation and rebound signals. *IEEE Transactions on Ultrasonics Ferroelectrics and Frequency Control*, Vol.53, No.1 (2006), pp.126-136.

(10) S.H. Chen, X.H. Chen, Y. Wang, K. Kosai, M.J. Finegold, S.S. Rich, S.L. Woo, Combination gene therapy for liver metastasis of colon carcinoma in vivo. *The Proceedings of the National Academy of Sciences of the United States of America*, Vol.92, No.7 (1995), pp.2577-2581.

(11) P.P. Kamaev, J.D. Hutcheson, M.L. Wilson, M.R. Prausnitz, Quantification of optison bubble size and lifetime during sonication dominant role of secondary cavitation bubbles causing acoustic bioeffects. *Journal of the Acoustical Society of America*, Vol.115, No.4 (2004), pp.1818-1825.

(12) J. Wu, J. Tong, Experimental study of stability of a contrast agent in an ultrasound field. *Ultrasound in Medicine and Biology*, Vol.24, No.2 (1998), pp.257-265.

(13) H.R. Guzman, D.X. Nguyen, S. Khan, M.R. Prausnitz, Ultrasound-mediated disruption of cell membranes. I. Quantification of molecular uptake and cell viability. *Journal of the Acoustical Society of America*, Vol.110, No.1 (2001), pp.588-596.

(14) A. van Wamel, K. Kooiman, M. Harteveld, M. Emmer, F.J. ten Cate, M. Versluis, N. de Jong, Vibrating microbubbles poking individual cells: drug transfer into cells via sonoporation. *Journal of Control Release*, Vol.112, No.2 (2006), pp.149-155.

(15) T. Li, K. Tachibana, M. Kuroki, Gene transfer with echo-enhanced contrast agents: comparison between Albunex, Optison, and Levovist in mice--initial results. *Radiology*, Vol.229, No.2 (2003), pp.423-428.

(16))X. Wang, H.D. Liang, B. Dong, Q.L. Lu, M.J. Blomley, Gene transfer with microbubble ultrasound and plasmid DNA into skeletal muscle of mice: comparison between commercially available microbubble contrast agents. *Radiology*, Vol.237, No.1 (2005), pp.224-229.

(17) H.R. Guzman, A.J. McNamara, D.X. Nguyen, M.R. Prausnitz, Bioeffects caused by changes in acoustic cavitation bubble density and cell concentration: A unified explanation based on cell-to-bubble ratio and blast radius. *Ultrasound in Medicine and Biology*, Vol.29, No.8 (2003), pp.1211-1222.

(18) M. Ward, J. Wu, J.F. Chiu, Experimental study of the effects of Optison concentration on sonoporation in vitro. *Ultrasound in Medicine and Biology*, Vol.26, No.7 (2000),

pp.1169-1175.

(19) E.N. Harvey, D.K. Barnes, W.D. McElroy, A.H. Whiteley, D.C. Pease, K.W. Cooper, Bubble formation in animals. *Journal of cellular and comparative physiology*, Vol.24 (1944), pp.1-22.

(20) R.E. Apfel, C.K. Holland, Gauging the likelihood of cavitation from short-pulse, low-duty cycle diagnostic ultrasound. *Ultrasound in Medicine and Biology*, Vol.17, No.2 (1991), pp.179-185.

(21) W.S. Chen, T.J. Matula, L.A. Crum, The disappearance of ultrasound contrast bubbles: observations of bubble dissolution and cavitation nucleation. *Ultrasound in Medicine and Biology*, Vol.28, No.6 (2002), pp.793-803.

(22) D.L. Miller, R.M. Thomas, Ultrasound contrast agents nucleate inertial cavitation in vitro. *Ultrasound in Medicine and Biology*, Vol.21, No.8 (1995), pp.1059-1065.

(23) D.M. Hallow, A.D. Mahajan, T.E. McCutchen, M.R. Prausnitz, Measurement and correlation of acoustic cavitation with cellular bioeffects. *Ultrasound in Medicine and Biology*, Vol.32, No.7 (2006), pp.1111-1122.

(24) D.M. Skyba, R.J. Price, A.Z. Linka, T.C. Skalak, S. Kaul, Direct in vivo visualization of intravascular destruction of microbubbles by ultrasound and its local effects on tissue. *Circulation*, Vol.98, No.4 (1998), pp.290-293.

(25) M.J. Shortencarier, P.A. Dayton, S.H. Bloch, P.A. Schumann, T.O. Matsunaga, K.W. Ferrara, A method for radiation-force localized drug delivery using gas-filled lipospheres. *IEEE Transactions on Ultrasonics, Ferroelectrics, and Frequency Control*, Vol.51, No.7 (2004), pp.822-831.

(26) T. Kodama, Y. Tomita, K. Koshiyama, M.J. Blomley, Transfection effect of microbubbles on cells in superposed ultrasound waves and behavior of cavitation bubble. *Ultrasound in Medicine and Biology*, Vol.32, No.6 (2006), pp.905-914.

(27) S. Gambihler, M. Delius, J.W. Ellwart, Permeabilization of the plasma-membrane of L1210 mouse leukemia-cells using lithotripter shock-waves. *Journal of Membrane Biology*, Vol.141, No.3 (1994), pp.267-275.

(28) T. Kodama, A.G. Doukas, M.R. Hamblin, Shock wave-mediated molecular delivery into cells. *Biochimica et Biophysica Acta*, Vol.1542, No.13 (2002), pp.186-194.

(29) A.G. Doukas, D.J. McAuliffe, T.J. Flotte, Biological effects of laser-induced shock waves: structural and functional cell damage in vitro. *Ultrasound in Medicine and Biology*, Vol.19, No.2 (1993), pp.137-146.

(30) T. Kodama, M.R. Hamblin, A.G. Doukas, Cytoplasmic molecular delivery with shock waves: importance of impulse. *Biophysical Journal*, Vol.79, No.4 (2000), pp.1821-1832.

(31) K. Koshiyama, T. Kodama, T. Yano, S. Fujikawa, Structural change in lipid bilayers and water penetration induced by shock waves: molecular dynamics simulations. *Biophysical Journal*, Vol.91, No.6 (2006), pp.2198-2205.

(32) K. Koshiyama, T. Kodama, T. Yano, S. Fujikawa, Molecular dynamics simulation of structural changes of lipid bilayers induced by shock waves: Effects of incident angles. *Biochimica et Biophysica Acta*, Vol.1778, No.6 (2008), pp.1423-1428.

(33) K. Koshiyama, T. Kodama, T. Yano, S. Fujikawa, Molecular dynamics simulation of water pore formation in lipid bilayer induced by shock waves. *Therapeutic Ultrasound: 5th International Symposium on Therapeutic Ultrasound*, Vol. 829, (2005), pp.583-587.

(34) A. Aoi, Y. Watanabe, S. Mori, M. Takahashi, G. Vassaux, T. Kodama, Herpes simplex virus thymidine kinase-mediated suicide gene therapy using nano/microbubbles and ultrasound. *Ultrasound in Medicine and Biology*, Vol.34, No.3 (2008), pp.425-434.

(35) J.R. Tennant, Evaluation of the trypan blue technique for determination of cell viability. *Transplantation*, Vol.2 (1964), pp.685-694.

(36))T. Kodama, A.G. Doukas, M.R. Hamblin, Delivery of ribosome-inactivating protein toxin into cancer cells with shock waves. *Cancer Letters*, Vol.189, No.1 (2003), pp.69-75.

(37) M. Postema, A. Bouakaz, M. Versluis, N. de Jong, Ultrasound-induced gas release from contrast agent microbubbles. *IEEE Transactions on Ultrasonics, Ferroelectrics, and Frequency Control*, Vol.52, No.6 (2005), pp.1035-1041.

(38) B. Wolfrum, R. Mettin, T. Kurz, W. Lauterborn, Observations of pressure-wave-excited contrast agent bubbles in the vicinity of cells. *Applied Physics Letters*, Vol.81, No.26 (2002), pp.5060-5062.

(39) C.D. Ohl, M. Arora, R. Ikink, N. de Jong, M. Versluis, M. Delius, D. Lohse, Sonoporation from jetting cavitation bubbles. *Biophysical Journal*, Vol.91, No.11 (2006), pp.4285-4295.

(40) J.R. Blake, B.B. Taib, G. Doherty, Transient cavities near boundaries .1. rigid boundary. *Journal of Fluid Mechanics*, Vol.170 (1986), pp.479-497.

(41) J.R. Blake, B.B. Taib, G. Doherty, Transient cavities near boundaries .2. free-surface. *Journal of Fluid Mechanics*, Vol.181 (1987), pp.197-212.

(42) A. Shima, K. Takayama, Y. Tomita, N. Miura, An experimental study on effects of a solid wall on the motion of bubbles and shock waves in bubble collapse. *Acustica*, Vol.48, No.5 (1981), pp.293-301.

(43) J.B. Keller, M. Miksis, Bubble oscillations of large amplitude. *Journal of the Acoustical Society of America*, Vol.68, No.2 (1980), pp.628-633.

(44) A. Prosperetti, A. Lezzi, Bubble Dynamics in a Compressible Liquid .1. 1st-Order Theory. *Journal of Fluid Mechanics*, Vol.168 (1986), pp.457-478.

(45) P.A. Dayton, J.E. Chomas, A.F.H. Lum, J.S. Allen, J.R. Lindner, S.I. Simon, K.W. Ferrara, Optical and acoustical dynamics of microbubble contrast agents inside neutrophils. *Biophysical Journal*, Vol.80, No.3 (2001), pp.1547-1556.

(46) J. Sundaram, B.R. Mellein, S. Mitragotri, An experimental and theoretical analysis of ultrasound-induced permeabilization of cell membranes. *Biophysical Journal*, Vol.84, No.5 (2003), pp.3087-3101.

(47) E.A. Evans, R. Waugh, L. Melnik, Elastic area compressibility modulus of red cell membrane. *Biophysical Journal*, Vol.16, No.6 (1976), pp.585-595.

(48) R. Hickling, M. Plesset, Collapse and rebound of a spherical bubble in water. *Physics of Fluids*, Vol.7, No.1 (1964), pp.7-14.

(49) R.H. Cole, Underwater Explosions, *Princeton University Press, Princeton, NJ*, (1948).

(50) Y. Tomita, M. Tsubota, N. An-Naka, Energy evaluation of cavitation bubble generation and shock wave emission by laser focusing in liquid nitrogen. *Journal of Applied Physics*, Vol.93, No.5 (2003), pp.3039-3048.

(51) B. Alberts, D. Bray, J. Lewis, M. Raff, K. Roberts, J.D. Watson, *Molecular biology of the cell,* Garland Publishing, Inc., New York & London, (1994).

(52) A.J. Yule, Y. Al-Suleimani, On droplet formation from capillary waves on a vibrating surface. *Proceedings of the Royal Society of London Series a-Mathematical Physical and Engineering Sciences*, Vol.456, No.1997 (2000), pp.1069-1085.

(53) S. Bao, B.D. Thrall, D.L. Miller, Transfection of a reporter plasmid into cultured cells by sonoporation in vitro. *Ultrasound in Medicine and Biology*, Vol.23, No.6 (1997), pp.953-959.

(54) T. Tsujino, A. Shima, The Behavior of Gas-Bubbles in Blood Subjected to an Oscillating Pressure. *Journal of Biomechanics*, Vol.13, No.5 (1980), pp.407-416.

(55) S. Fujikawa, T. Akamatsu, Effects of the non-equilibrium condensation of vapour on the pressure wave produced by the collapse of a bubble in a liquid. *Journal of Fluid Mechanics*, Vol.97, No.3 (1980), pp.481-512.

(56) Y. Tomita, A. Shima, On the behavior of a spherical bubble and the impulse pressure in a viscous compressible liquid. *Bulletin of the JSME*, Vol.20, No.149 (1977), pp.1453-1460.

(57) C. Chiba, Study on atomization of liquid due to ultrasound oscillation. *Ph.D. Thesis, Engineering, Tohoku University, Sendai*, (1983).

Biochimica et Biophysica Acta 1778 (2008) 1423–1428

Contents lists available at ScienceDirect

Biochimica et Biophysica Acta

journal homepage: www.elsevier.com/locate/bbamem

Molecular dynamics simulation of structural changes of lipid bilayers induced by shock waves: Effects of incident angles

Kenichiro Koshiyama [a,*], Tetsuya Kodama [b], Takeru Yano [c], Shigeo Fujikawa [d]

[a] Graduate School of Engineering Science, Osaka University, Toyonaka, 560-8531, Japan
[b] Graduate School of Biomedical Engineering, Tohoku University, Sendai, 980-8575, Japan
[c] Graduate School of Engineering, Osaka University, Suita, 565-0871, Japan
[d] Graduate School of Engineering, Hokkaido University, Sapporo, 060-8628, Japan

ARTICLE INFO

Article history:
Received 12 November 2007
Received in revised form 7 March 2008
Accepted 12 March 2008
Available online 20 March 2008

Keywords:
Acoustic wave
Cell membrane permeabilization
Impulse
Shear force
Sonoporation
Ultrasound

ABSTRACT

Unsteady and nonequilibrium molecular dynamics simulations of the response of dipalmitoylphosphatidylcholine (DPPC) bilayers to the shock waves of various incident angles are presented. The action of an incident shock wave is modeled by adding a momentum in an oblique direction to water molecules adjacent to a bilayer. We thereby elucidate the effects of incident shock angles on (i) collapse and rebound of the bilayer, (ii) lateral displacement of headgroups, (iii) tilts of lipid molecules, (iv) water penetration into the hydrophobic region of the bilayer, and (v) momentum transfer across the bilayer. The number of water molecules delivered into the hydrophobic region is found to be insensitive to incident shock angles. The most important structural changes are the lateral displacement of headgroups and tilts of lipid molecules, which are observed only in the half of the bilayer directly exposed to a shock wave for all incident shock angles studied here. As a result, only the normal component of the added oblique momentum is substantially transferred across the bilayer. This also suggests that the irradiation by shock waves may induce a jet-like streaming of the cytoplasm toward the nucleus.

1. Introduction

The cell membrane permeabilization technique utilizing mechanical forces due to high-intensity acoustic waves (shock wave or ultrasound) is a promising method of noninvasive drug and gene delivery into the cytoplasm [1–5]. For the last decade, several authors have addressed the permeabilization mechanisms, in vitro and in vivo, which are fundamental for the complete development of drug and gene delivery methods based on shock waves or ultrasound [6–14]. They have reported that cavitation-induced nonthermal effects (e.g., radiation force, micro-streaming, micro-jets, or shock waves from cavitation bubbles) can induce reversible lesions of cell membranes, and the cell membranes are thereafter permeabilized [6–14].

The above mentioned studies are limited to the macroscopic or cellular level. At the microscopic or molecular level, on the other hand, the mechanisms of the permeabilization induced by shock waves or ultrasound are not well understood. Recently, we conducted molecular dynamics (MD) simulations of the structural changes of phospholipid bilayers of cell membranes induced by the action of shock waves [15]. One of the important findings was that the resulting collapse and rebound of a bilayer are followed by the penetration of water molecules into the hydrophobic region of the bilayer.

In the simulations, the propagation direction of the applied incident shock waves was parallel to the bilayer normal direction. However, bilayers are generally undulating on a length scale well beyond their thickness [16]. That is, the incident shock angles on the membrane surface practically vary with the location on the surface where the shock wave impacts. Furthermore, a numerical analysis in fluid dynamics [17] points out that an oblique impact of a shock wave induces a kind of shear flow around cell membranes and the forces resulting from the flow field are responsible for cell deformation and lysis. The effects of the incident shock angles on the structural changes of a lipid bilayer underlie the permeabilization mechanisms at the molecular level. Therefore, the objective of this study is to analyze the structural changes of a lipid bilayer by using the shock waves of various incident shock angles.

The foundation of all biological membranes is the lipid bilayer structure consisting of two leaflets of phospholipids. Thus, their dynamics (i.e., rearrangement of the phospholipids) is central to understanding the behavior of biological membranes. MD simulations of lipid bilayers have provided accurate models of biological membranes at the nanometer and nanosecond scales [18–21], and the molecular behaviors of lipids, water, and membrane proteins in equilibrium states have been clarified [18,22–25]. Moreover, the studies on the lipid bilayer responses to surface area changes [26], mechanical stresses [27], electric fields [28–30], and shear flows [31–33] are beginning to be conducted.

* Corresponding author. Department of Mechanical Science and Bioengineering, Graduate School of Engineering Science, Osaka University, Toyonaka, 560-8531, Japan. Tel.: +81 6 6850 6173; fax: +81 6 6850 6172.
E-mail address: koshiyama@me.es.osaka-u.ac.jp (K. Koshiyama).

0005-2736/$ – see front matter © 2008 Elsevier B.V. All rights reserved.
doi:10.1016/j.bbamem.2008.03.010

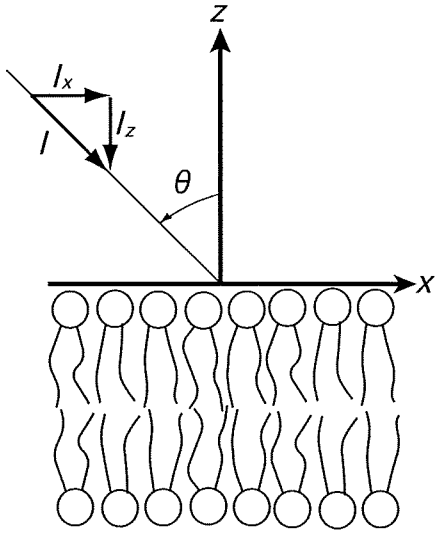

Fig. 1. Schematic diagram of the interaction of a shock wave with a lipid bilayer, where θ is the incident angle between the bilayer normal and the direction of shock wave propagation.

However, these studies involve responses in the steady or almost steady states. We emphasize that a shock wave is a high-pressure wave with a steep wave front that propagates at a supersonic speed, and it passes the cell membrane within a very short time of the order of picoseconds. Therefore, understanding the high-speed phenomenon induced by the interaction of a shock wave with a lipid bilayer should be indispensable. We address the lipid bilayer responses not to steady but unsteady actions induced by shock waves, particularly focusing on the effect of various incident shock angles.

In the previous study [15], we have modeled a shock wave by its impulse and performed unsteady and nonequilibrium MD simulations. Here, we slightly modify the shock wave impulse model to take account of incident shock angles, and the modified model is described in the Methods section. In the Results section, the collapse stage and the rebound stage are defined, and then the lateral displacement of headgroups, tilts of lipid molecules, water penetration into the hydrophobic region of a bilayer, and the momentum transfer across the bilayer are analyzed in detail. We finally summarize the effects of incident shock angles on the structural changes of a bilayer and discuss possible streaming in the cytoplasm induced by shock waves in the Summary and discussion section.

2. Methods

2.1. Lipid bilayer system

In this study, we investigated the effect of the incident angle of a shock wave on a lipid bilayer distributed on a plane surface (see Fig. 1). The lipid bilayer system comprised 128 DPPC molecules fully hydrated by 16455 water molecules. For equilibration, we performed 20-ns simulations with our force fields (see below) in a constant *NPT* ensemble, and we obtained the equilibrated bilayer system of volume $6.56\times6.40\times15.90$ nm^3, where the linear dimension of the simulation box in the z direction normal to the bilayer plane (the xy plane) is 15.90 nm. The detailed simulation procedures for the bilayer equilibration are summarized elsewhere [15,19]. We remark that our system included a large water layer of thickness about 12 nm, whereas the thickness of the bilayer was about 4 nm. This is because this simulation of a shock wave required a large number of water molecules, as explained below.

The force fields for DPPC and water were consistent with those employed in the previous study [15], which includes the refined united atom force field with AMBER99 force field [19] and single point charge (SPC) model [34]. The partial charges of a DPPC molecule were obtained from the study by Chiu et al. [35]. Because we are interested in the dynamical process of a structural change in a bilayer resulting from shock wave irradiation, it may be better to remove the constraints of molecular bond lengths, angles, and dihedrals. Therefore, all bonded interactions in DPPC molecules were calculated in the shock wave simulation. The particle mesh Ewald method [36] was used to treat the long-range electrostatic interactions. Both the real-space Ewald and the van der Waals nonbonded interactions were cut off at 1.0 nm. The AMBER 8 set of programs [37] was used for computations.

2.2. Shock wave impulse simulation

As demonstrated in the previous study [15], we modeled a shock wave by its impulse I defined as the time integral of pressure over the shock-pulse duration [7]. From the definition of the impulse, the shock impulse I can be regarded as an increment in the momentum of water divided by an area A on which the shock pressure is exerted. The momentum increment is numerically implemented by the addition of the average velocity V to the thermal velocity of water molecules in a slab adjacent to a bilayer. V is given by

$$V = \frac{I \times A}{mN_W}, \tag{1}$$

where m is the weight of a water molecule and N_W is the number of water molecules in the water slab.

Because the choice of a water slab is arbitrary, we consider the water slab of $A\times L_z$, where $A=42.2$ nm^2 was the area of the xy plane of the bilayer system and $L_z=4.0$ nm was the thickness of the water slab. We set $I=40$ mPa·s and the number of water molecules in the water slab $N_W=5423$; the applied average velocity V was 10,394 m/s. Note that V corresponds neither to the sound speed in liquid water nor to the propagation speed of the shock wave. It just represents the increase in the momentum of water molecules due to the shock wave.

In the present study, we slightly modified the shock wave model described above to take account of the incident shock angle. More precisely, the shock wave impulse was divided into the normal (in the z direction) and tangential (in the x direction) components to the bilayer plane (see Fig. 1). That is,

$$I_z = I\cos\theta \quad \text{and} \quad I_x = I\sin\theta, \tag{2}$$

where I_z is the normal component; I_x, the tangential component; and θ, the incident shock angle. V was decomposed to the normal component $V_z=V\cos\theta$ and the tangential component $V_x=V\sin\theta$.

For understanding high-speed and unsteady phenomenon induced by a shock wave impulse in MD, position and velocity scaling of molecules should not be implemented. Therefore, we performed constant *NVE* MD simulation without using the temperature and pressure controls and bond constraints from the initial configuration. The constant energy in this MD is the sum of the total energy in the equilibrium state and the kinetic energy increase induced by adding velocity. Periodic boundary conditions were applied in the three directions. The time step used for the integration of equations of motion was 0.2 fs in order to avoid the excess approach of molecules with large velocities. Owing to the periodic boundary conditions, the simulations were terminated at the time when the effect of the shock impulse reached the boundary at the opposite side of the simulation box in the z direction. This is the reason why we prepared a thick water layer. The numerical results shown in the following are the sample averages of 10 production runs for a given θ. From the results of the previous study and preliminary calculations, the system size and the simulation time in the present study were determined in order to focus on the analysis of the essential part of the structural changes in unsteady states.

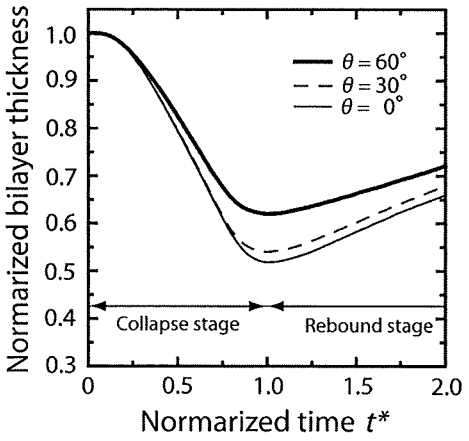

Fig. 2. Temporal changes of the bilayer thickness in the simulations for θ=0°, 30°, and 60°. The bilayer thickness is normalized by that in the initial state (ca. 4.0 nm). Note that in the following figures the normalized time $t^*=1$ corresponds to 530, 590, and 810 fs in real time for θ=0°, 30°, and 60°, respectively.

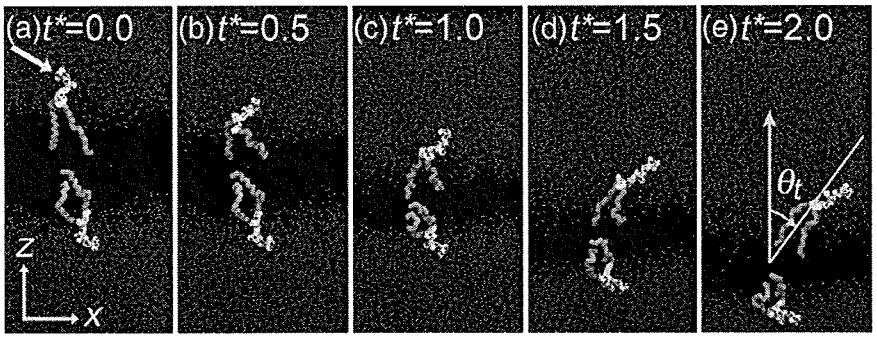

Fig. 3. Snapshots of postural changes of typical lipid molecules in upper and lower layers induced by the shock wave with θ=60°. The yellow bars represent the headgroup of a lipid molecule; the orange bars, the hydrophobic chains; and the red spheres, water molecules. The yellow arrow in the snapshot of t^*=0 denotes the propagation direction of the incident shock wave. The other lipid molecules are eliminated for clarity.

2.3. Analysis

The changes of hydrophobic chains in the unsteady states can be explained in terms of an averaged instantaneous chain order parameter $\hat{S}_{CD}$ [15],

$$\hat{S}_{CD} = -\frac{1}{2}\left(\frac{1}{N_C}\sum_{i=1}^{N_C}\frac{1}{2}(3\cos^2\Theta_i - 1)\right), \tag{3}$$

where Θ_i is the angle between the axis of the ith molecular axis and the bilayer normal (the z axis) and N_C (=28) is the number of carbons in both *sn*-1 and *sn*-2 chains. Θ_i is evaluated from the instantaneous configurations of lipid molecules. Note that Θ_i in the upper layer is calculated with respect to the bilayer director as pointed out in Ref. [31], because the lipid molecules in the upper layer tilt (see the Results section).

The lateral movement of lipid molecules is characterized by the averaged lateral displacement of the mass center positions of the headgroups of lipid molecules $L(t)$ defined by

$$L(t) = \frac{1}{N_L}\sum_{i=1}^{N_L}|x_i(t) - x_i(0)|, \tag{4}$$

where x_i is the x coordinate of the mass center position of the headgroup of the ith molecule, and N_L(=64) is the number of DPPC molecules in the upper or lower layer.

3. Results

3.1. Collapse and rebound of bilayers

The most outstanding change in a bilayer by the action of a shock wave is the change in the bilayer thickness, which is defined as the distance between the phosphorus atoms of lipid molecules in the upper and lower layers [15]. Fig. 2 shows the temporal changes of the bilayer thickness caused by the shock wave impulses of 40 mPa·s for θ=0°, 30°, and 60°. The bilayer thickness became minimum at 530, 590, and 810 fs for θ=0°, 30°, and 60°, respectively. The normalized time t^* in Fig. 2 is defined such that the minimum of bilayer thickness occurs at t^*=1. That is, the bilayer thickness is decreasing during $0<t^*<1$ (i.e., collapse stage); then, the bilayer thickness starts to increase after t^*=1 (i.e., rebound stage) regardless of the incident shock angle conditions. In the following the normalized time t^*=1 corresponds to 530, 590, and 810 fs in real time for θ=0°, 30°, and 60°, respectively.

In each incident angle condition, the duration of the rebound stage ($1<t^*$) is longer than that of the collapse stage ($0<t^*<1$). The rebound stage was not completed within the present simulation because of the periodic boundary conditions (see the Methods section). However, the essential points can be clarified as demonstrated below.

The change in the bilayer thickness is expected to be due to the postural changes of lipid molecules. In Fig. 3, we show a series of snapshots of postural changes of typical lipid molecules in the upper and lower layers induced by the shock wave with θ=60°. By the action of the shock wave, the hydrophobic chains bend (Fig. 3(a)–(c)) and then slightly recover (Fig. 3(d) and (e)). Fig. 4 shows temporal changes of $\hat{S}_{CD}$ for θ=60°, normalized by those in the initial state (ca. −0.16). The order parameters obviously decrease in the collapse stage and gradually recover in the rebound stage. On comparison with the result in Fig. 2, it is confirmed that the decrease in the bilayer thickness was due to this chain disorder. This result is consistent with the previous simulation result [15].

3.2. Lateral movement of lipid molecules

The oblique incidence of a shock wave yields unsteady shear on the bilayer surface. In this simulation, the shear is induced by the tangential momentum change of water molecules adjacent to the bilayer surface (see the Methods section). In Fig. 3, the effect of shear appears as the lateral movement of the lipid molecules in the upper layer. Fig. 5 shows the time evolution of the averaged lateral displacements in the upper and lower layers. As pointed out in the previous study [15], the simple shock wave interaction (θ=0°) enhances the lateral displacement. However, the displacement in the upper layer significantly increases with the incident shock angle from 0° to 60°. In fact, the displacement induced by the shock wave with θ=60° becomes 1.5 nm at t^*=2, which is ten times larger than that with θ=0°. Here, we remark that the lateral displacements of lipid molecules for θ=30° and 60° continue to increase even in the rebound stage. On the other hand, the lateral displacement in the lower layer is one order of magnitude smaller than that in the upper layer (Fig. 5 inset).

3.3. Tilt of lipid molecules

From the snapshots in Fig. 3, it is clear that the lipid molecule in the upper layer tilts by the action of incident shock wave. Here, we define the tilt angle as follows: (i) atom positions of a lipid molecule are projected onto the xz plane; (ii) a straight line is fitted to these projected

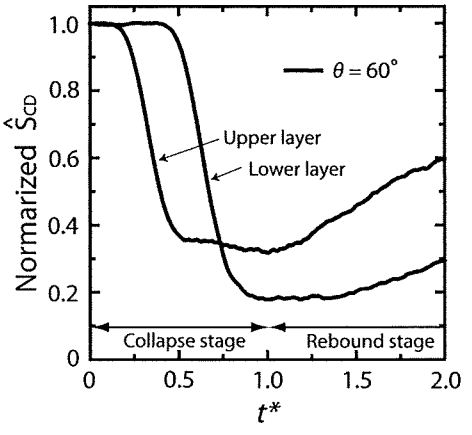

Fig. 4. Temporal changes of averaged instantaneous order parameter for θ=60°. The order parameters are normalized by those in the initial state.

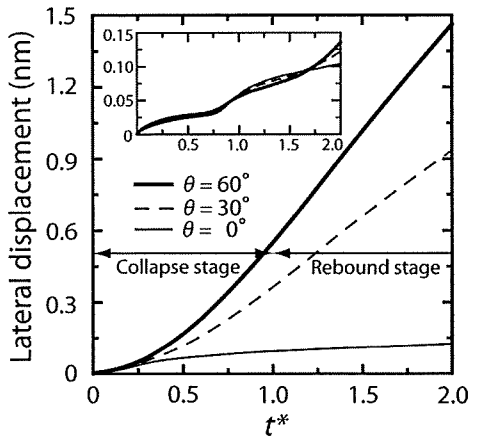

Fig. 5. Lateral displacement of the mass center of lipid headgroups for θ=0°, 30°, and 60° in the upper layer and that in the lower layer (inset).

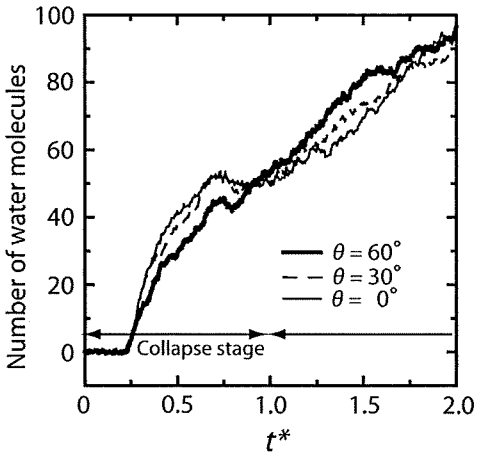

Fig. 7. Number of the water molecules delivered into the hydrophobic region of a bilayer induced by shock wave with θ=0°, 30°, and 60°.

positions; (iii) the tilt angle θ_t is obtained from the angle formed between this straight line and the z axis (see Fig. 3(e)). The tilt angle in the initial state (t^*=0) calculated here has a wide distribution centered around zero degree, which would be tantamount to that in the equilibrium state of another study [24] although they used a different force field and their tilt angle is defined as that between a vector formed by alternating carbon units along the lipid tails and the bilayer normal axis.

Fig. 6(a) shows the tilt angle distributions of the lipid molecules in the upper layer at t^*=2. In the case of θ=0°, the distribution of tilt angles is hardly changed from that in the initial state. On the contrary, the distributions for θ=30° and 60° shift to the positive side. In Fig. 6 (b), we show the temporal changes of the tilt angles averaged for all lipid molecules in the upper layer. Obviously, the averaged tilt angles for θ=30° and 60° increase with time and reach maximum values at around t^*=2 (21°, and 32°, respectively). The maximum values are in agreement with those in Ref. [31] on the interaction of steady shear flows with lipid bilayers. In the present unsteady simulation, the lipid alignment is completed within t^*=2. Thus, the simulation

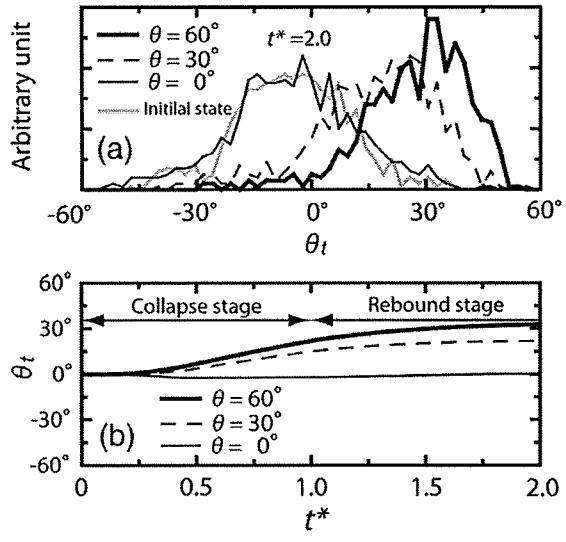

Fig. 6. (a) Tilt angle distributions of the lipid molecules in the upper layer for θ=0°, 30°, and 60° at t^*=2.0 (b) Temporal changes of the averaged tilt angle of lipid molecules in the upper layer. Note that the average equilibrium angle in the initial state is taken as 0° in (b).

limited to $0<t^*<2.0$ is adequate to analyze the essential part of the structural changes in unsteady states. Interestingly, whereas the lateral movement of lipid molecules persists as shown in Fig. 5, their tilts are saturated (Fig. 6(b)). However, this will not be discussed in this paper.

The tilt angles averaged in the lower layer did not change (data not shown). We emphasize that this is not due to the restriction of simulation time because the steady simulation of shear flow also obtained the same result [31].

3.4. Water penetration into the hydrophobic region

In the equilibrium state water molecules hardly exist in the hydrophobic region [18] and the event of water penetration into the hydrophobic region rarely occurs in the time scale of MD simulations [38,39]. On the other hand, under the action of shock waves the water penetration into the hydrophobic region was observed in the time scale of picoseconds (see Fig. 3), which is important for subsequent water pore formation in a bilayer [40] and cell membrane permeabilization [4,6,9,15]. Fig. 7 shows the temporal changes of the number of water molecules delivered into the hydrophobic region for θ=0°, 30°, and 60°. Here, the hydrophobic region is defined as the region between the carbonyl groups in *sn*-1 chains in the upper and lower layers [15]. Most of the water molecules penetrated are from the upper water layer. The water penetration in the intermediate stage of

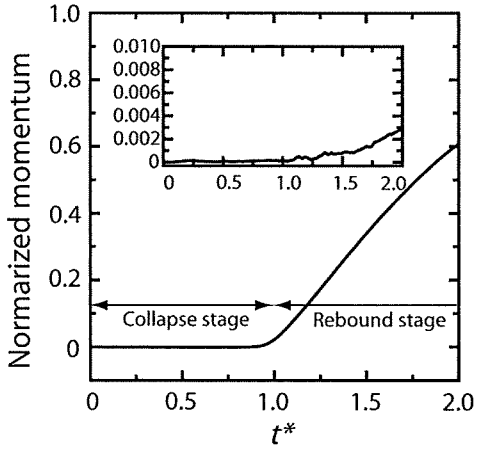

Fig. 8. Temporal changes of the momentum of the lower water layer in the z direction (normal component) and that in the x direction (tangential component, inset) for θ=60°.

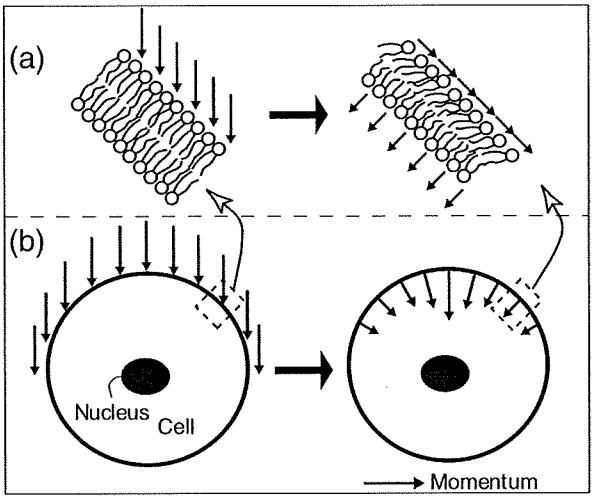

Fig. 9. Schematic diagram of (a) structural changes of cell membranes and (b) expected momentum transfer across the membrane in a cell by shock waves.

the collapse stage ($0.25<t^*<0.75$) is smaller in the larger incident angle condition. By contrast, in the intermediate stage of the rebound stage ($1.25<t^*<1.75$), the water penetration is larger in the larger incident angle condition. As a result, the total number of delivered water molecules amounts to almost 100 for all cases of $\theta=0°$, 30°, and 60°, indicating the fact that the water penetration in $0<t^*<2.0$ is insensitive to the incident angles, at least for the case of $I=40$ mPa·s.

The trend in the collapse stage is clearly a direct consequence of the difference in the impulse intensity in the normal direction. In the rebound stage, on the other hand, a large amount of the normal component of the momentum has been transferred through the upper layer, as shown in the next subsection; instead, the lateral displacements and tilts of lipid molecules in the upper layer are prominent as demonstrated in Figs. 5, and 6. Therefore, the penetration of water molecules near the upper layer in the rebound stage may be governed by these lipid structural changes [23,25,41].

3.5. Momentum transfer across bilayers

It is interesting to assess the amount of momentum transferred across the bilayer by the shock wave because the momentum transfer is related to the transfer characteristics of the bilayer or a subsequent flow induction. The momentum transfer can be estimated from the changes of momentum in the lower water layer. In Fig. 8, we show temporal changes of the normal and tangential components of momentum for $\theta=60°$ normalized by the corresponding values initially added to the water slab. Both the components begin to increase at around $t^*=1.0$, and in particular, the normal component attains 60% of its initial value at $t^*=2.0$, while the increase in the tangential component remains very small. That is, only the normal component of the added oblique momentum is substantially transferred across the bilayer within the time scale of the order of picoseconds. This certainly affects the flow induction in the cytoplasm and this will be discussed in detail in the final section. Note that the rest of the normal component, 40% of its initial value, still stays inside the bilayer at $t^*=2.0$ as can be seen from Fig. 3(e), where the downward movement of lipid molecules persists.

The ratio between the sliding force per unit of bilayer area and the velocity difference between the two leaflets of a bilayer is called the intermonolayer friction coefficient b, which is one of the measures of the intermonolayer flow behavior [32,33,42]. b is given by $b=F/A\Delta V$, where F is the sliding force, A is the bilayer area, and ΔV is the velocity difference. Usually, b is evaluated in lengthy steady simulations, however, it can be obtained in an unsteady simulation as follows: F for $\theta=60°$ was roughly calculated from the momentum change of the lower layer (17753.06 N·s/mol) divided by the time interval $0<t^*<2.0$ (1.56 ps); the sliding force between the lower monolayer and lower water layer was assumed to be zero because of the very small amount of momentum transferred to the lower water layer (Fig. 8 inset); the slip velocity was the instantaneous velocity difference of the mass centers of the upper and lower layers at $t^*=2.0$ (571.74 m/s). As a result, we obtained $b=8\times10^5$ Pa m^{-1}s at $t^*=2.0$ in the unsteady state using the present simulation results. Surprisingly, the intermonolayer friction coefficient in the present study is almost the same as that obtained in the coarse-grained MD simulations in Refs. [32,33] (typically 1×10^6 Pa m^{-1}s) by applying Lees–Edwards boundary conditions, although the normal component of momentum was not considered in these simulations.

4. Summary and discussion

This study aimed at investigating the effect of incident shock angles on the structural changes of a lipid bilayer by using unsteady nonequilibrium MD simulations. The simulation results revealed that the half of the bilayer directly exposed to shock waves is sensitive to an incident shock wave; therefore, the lateral displacement and the tilts of lipid molecules are enhanced with an increase in the incident shock angle from 0° to 60° within the time scale of the order of picoseconds (Fig. 9(a)). On the other hand, the other half of the bilayer is found to be insensitive to the change of the incident shock angle. This difference in sensitivity to the incident shock wave results in the fact that only the normal component of the applied oblique impulse is transferred across the bilayer.

Finally, we discuss the possible streaming of the cytoplasm induced by shock waves. As shown in Fig. 8, the normal component of the applied momentum promptly transfers across the bilayer, whereas the tangential component hardly transfers. Here, let us assume a cell to be a sphere and a shock wave impulse is applied downward on the surface of the sphere (Fig. 9(b) left). The intensity of the applied momentum along membrane normal is largest on the top of the sphere, and it is reduced to zero along the meridian of the sphere. Accordingly, the momentum distribution has a maximum (Fig. 9(b) right), which will result in the formation of a jet-like streaming in the cytoplasm. In reality, the cell membrane is usually undulating; hence, several momentum maxima with different directions may be produced beneath the membrane. Therefore, the streaming in the cytoplasm caused by the shock wave will be comprised of several jet-like flows emerged from several momentum maxima, and the entire flow pattern in the cytoplasm will become complex. The mixing or homogenization of plasmid [10] and fluorescein [7] throughout the cell cytoplasm appears to be enhanced by jet-like flows.

Acknowledgements

TK acknowledges (i) the Encouraging Development of Strategic Research Center, Special Coordination Funds for Promoting Science and Technology, MEXT, Japan, (ii) Grant-in-Aid for Scientific Research (B) (17300168), (iii) Grant-in-Aid for Exploratory Research (18650140), and (iv) Research on Advanced Medical Technology, The Ministry of Health Labor and Welfare (H19-nano-010).

References

[1] S. Gambihler, M. Delius, Transient increase in membrane permeability of L1210 cells upon exposure to lithotripter shock waves in vitro, Naturwissenschaften 79 (1992) 328–329.
[2] S. Gambihler, M. Delius, J.W. Ellwart, Permeabilization of the plasma membrane of L1210 mouse leukemia cells using lithotripter shock waves, J. Membr. Biol. 141 (1994) 267–275.
[3] U. Lauer, E. Burgelt, Z. Squire, K. Messmer, P.H. Hofschneider, M. Gregor, M. Delius, Shock wave permeabilization as a new gene transfer method, Gene Ther. 4 (1997) 710–715.

[4] L.B. Feril, T. Kondo, S. Umemura, K. Tachibana, H.A. Manalo, P. Riesz, Sound wave and antineoplastic drugs: the possibility of an enhanced combined anticancer therapy, J. Med. Ultrasonics 29 (2002) 173–187.
[5] S. Mehier-Humbert, R.H. Guy, Physical methods for gene transfer: improving the kinetics of gene delivery into cells, Adv. Drug Delivery Rev. 57 (2005) 733–753.
[6] M. Kambe, N. Ioritani, R. Kanamaru, Enhancement of chemotherapeutic effects with focused shock waves: extracorporeal shock wave chemotherapy (ESWC), Hum. Cell 10 (1997) 87–94.
[7] T. Kodama, M.R. Hamblin, A.G. Doukas, Cytoplasmic molecular delivery with shock waves: importance of impulse, Biophys. J. 79 (2000) 1821–1832.
[8] J. Sundaram, B.R. Mellein, S. Mitragotri, An experimental and theoretical analysis of ultrasound-induced permeabilization of cell membranes, Biophys. J. 84 (2003) 3087–3101.
[9] S. Mehier-Humbert, T. Bettinger, F. Yan, R.H. Guy, Plasma membrane poration induced by ultrasound exposure: implication for drug delivery, J. Contr. Rel. 104 (2005) 213–222.
[10] S. Mehier-Humbert, T. Bettinger, F. Yan, R.H. Guy, Ultrasound-mediated gene delivery: kinetics of plasmid internalization and gene expression, J. Contr. Rel. 104 (2005) 203–211.
[11] T. Kodama, Y. Tomita, K.I. Koshiyama, M.J.K. Blomley, Transfection effect of microbubbles on cells in superposed ultrasound waves and behavior of cavitation bubble, Ultrasound in Med. Biol. 32 (2006) 905–914.
[12] W.D. O'Brien Jr., Ultrasound-biophysics mechanisms, Prog. Biophys. Mol. Biol. 93 (2007) 212–255.
[13] D.L. Miller, Overview of experimental studies of biological effects of medical ultrasound caused by gas body activation and inertial cavitation, Prog. Biophys. Mol. Biol. 93 (2007) 314–330.
[14] E. VanBavel, Effects of shear stress on endothelial cells: possible relevance for ultrasound applications, Prog. Biophys. Mol. Biol. 93 (2007) 374–383.
[15] K. Koshiyama, T. Kodama, T. Yano, S. Fujikawa, Structural change in lipid bilayer and water penetration induced by shock wave: molecular dynamics simulations, Biophys. J. 91 (2006) 2198–2205.
[16] U. Seifert, Configurations of fluid membranes and vesicles, Adv. Phys. 46 (1997) 13–137.
[17] M. Lokhandwalla, B. Sturtevant, Mechanical haemolysis in shock wave lithotripsy (SWL): I. Analysis of cell deformation due to SWL flow-fields, Phys. Med. Biol. 46 (2001) 413–437.
[18] D.P. Tieleman, S.J. Marrink, H.J.C. Berendsen, A computer perspective of membranes: molecular dynamics studies of lipid bilayer systems, Biochim. Biophys. Acta-Rev. Biomemb. 1331 (1997) 235–270.
[19] A.M. Smondyrev, M.L. Berkowitz, United atom force field for phospholipid membranes: constant pressure molecular dynamics simulation of dipalmitoylphosphatidicholine/water system, J. Comp. Chem. 20 (1999) 531–545.
[20] C. Anezo, A.H. de Vries, H.D. Holtje, D.P. Tieleman, S.J. Marrink, Methodological issues in lipid bilayer simulations, J. Phys. Chem., B 107 (2003) 9424–9433.
[21] M. Patra, M. Karttunen, M.T. Hyvonen, E. Falck, P. Lindqvist, I. Vattulainen, Molecular dynamics simulations of lipid bilayers: major artifacts due to truncating electrostatic interactions, Biophys. J. 84 (2003) 3636–3645.
[22] W.L. Ash, M.R. Zlomislic, E.O. Oloo, D.P. Tieleman, Computer simulations of membrane proteins, Biochim. Biophys. Acta-Rev. Biomemb. 1666 (2004) 158–189.
[23] M. Kupiainen, E. Falck, S. Ollila, P. Niemela, A.A. Gurtovenko, M.T. Hyvonen, M. Patra, M. Karttunen, I. Vattulainen, Free volume properties of sphingomyelin, DMPC, DPPC, and PLPC bilayers, J.Comp. Theor. Nanosci. 2 (2005) 401–413.
[24] S. Leekumjorn, A.K. Sum, Molecular studies of the gel to liquid-crystalline phase transition for fully hydrated DPPC and DPPE bilayers, Biochim. Biophys. Acta-Biomemb. 1768 (2007) 354–365.
[25] K. Murzyn, W. Zhao, M. Karttunen, M. Kurdziel, T. Rog, Dynamics of water at membrane surfaces: effect of headgroup structure, Biointerphases 1 (2006) 98–105.
[26] J.G. Jeon, G.A. Voth, The dynamic stress responses to area change in planar lipid bilayer membranes, Biophys. J. 88 (2005) 1104–1119.
[27] H. Leontiadou, A.E. Mark, S.J. Marrink, Molecular dynamics simulations of hydrophilic pores in lipid bilayers, Biophys. J. 86 (2004) 2156–2164.
[28] D.P. Tieleman, The molecular basis of electroporation, BMC Biochem. 5 (2004) 1–10.
[29] Q. Hu, S. Viswanadham, R.P. Joshi, K.H. Schoenbach, S.J. Beebe, P.F. Blackmore, Simulations of transient membrane behavior in cells subjected to a high-intensity ultrashort electric pulse, Phys. Rev., E 71 (2005) 0319141–0319149.
[30] M. Tarek, Membrane electroporation: a molecular dynamics simulation, Biophys. J. 88 (2005) 4045–4053.
[31] P.D. Blood, G.S. Ayton, G.A. Voth, Probing the molecular-scale lipid bilayer response to shear flow using nonequilibrium molecular dynamics, J. Phys. Chem., B 109 (2005) 18673–18679.
[32] S.A. Shkulipa, W.K. den Otter, W.J. Briels, Surface viscosity, diffusion, and intermonolayer friction: simulating sheared amphiphilic bilayers, Biophys. J. 89 (2005) 823–829.
[33] W.K. den Otter, S.A. Shkulipa, Intermonolayer friction and surface shear viscosity of lipid bilayer membranes, Biophys. J. 93 (2007) 423–433.
[34] H.J.C. Berendsen, J.P.M. Postma, W.F. Gunsteren, J. Hermans, Interaction models for water in relation to protein hydration, in: B. Pullman (Ed.), Intermolecular Forces, D. Reidel Publishing Company, 1981, pp. 331–342.
[35] S.W. Chiu, M. Clark, V. Balaji, S. Subramaniam, H.L. Scott, E. Jakobsson, Incorporation of surface-tension into molecular-dynamics simulation of an interface — a fluid-phase lipid bilayer-membrane, Biophys. J. 69 (1995) 1230–1245.
[36] U. Essmann, L. Perera, M.L. Berkowitz, T. Darden, H. Lee, L.G. Pedersen, A smooth particle mesh Ewald method, J. Chem. Phys. 103 (1995) 8577–8593.
[37] D.A. Pearlman, D.A. Case, J.W. Caldwell, W.S. Ross, T.E. Cheatham, S. Debolt, D. Ferguson, G. Seibel, P. Kollman, Amber, a package of computer-programs for applying molecular mechanics, normal-mode analysis, molecular-dynamics and free-energy calculations to simulate the structural and energetic properties of molecules, Comp. Phys. Comm. 91 (1995) 1–41.
[38] S.J. Marrink, H.J.C. Berendsen, Simulation of water transport through a lipid-membrane, J. Phys. Chem. 98 (1994) 4155–4168.
[39] T.X. Xiang, Translational diffusion in lipid bilayers: dynamic free-volume theory and molecular dynamics simulation, J. Phys. Chem., B 103 (1999) 385–394.
[40] K. Koshiyama, T. Kodama, T. Yano, S. Fujikawa, Molecular dynamics simulation of water pore formation in lipid bilayer induced by shock waves, AIP Conf. Proc. 829 (2006) 583–587.
[41] J. Repakova, P. Capkova, J.M. Holopainen, I. Vattulainen, Distribution, orientation, and dynamics of DPH probes in DPPC bilayer, J. Phys. Chem., B 108 (2004) 13438–13448.
[42] E. Evans, A. Yeung, Hidden dynamics in rapid changes of bilayer shape, Chem. Phys. Lipids 73 (1994) 39–56.

Int. J. Cancer: **124**, 2505–2511 (2009)

FAST TRACK

Potent antitumor effect of SN-38-incorporating polymeric micelle, NK012, against malignant glioma

Jun-ichiro Kuroda[1,2], Jun-ichi Kuratsu[2], Masahiro Yasunaga[1], Yoshikatsu Koga[1], Yohei Saito[1] and Yasuhiro Matsumura[1]*

[1]*Investigative Treatment Division, Research Center for Innovative Oncology, National Cancer Center Hospital East, Kashiwa, Japan*
[2]*Department of Neurosurgery, Faculty of Medical and Pharmaceutical Sciences, Kumamoto University, Kumamoto, Japan*

Recent published reports on clinical trials of CPT-11 indicate the effectiveness of this compound, a prodrug of SN-38, against malignant glioma in combination with anti-vascular endothelial growth factor antibody. Here, we determined if NK012, and SN-38 incorporating micelle, can be an appropriate formulation for glioblastoma treatment compared with CPT-11. *In vitro* cytotoxicity was evaluated against several glioma lines with NK012, CPT-11, SN-38, ACNU, CDDP and etoposide. For the *in vivo* test, a human glioma line (U87MG) transfected with the *luciferase* gene was inoculated into nude mice brain for pharmacokinetic analysis by fluorescence microscopy and high-performance liquid chromatography after intravenous injection of NK012 and CPT-11. *In vivo* antitumor activity of NK012 and CPT-11 was evaluated by bioluminescence image and Kaplan-Meier analyses. The growth-inhibitory effects of NK012 were 34- to 444-fold more potent than those of CPT-11. Markedly enhanced and prolonged distribution of free SN-38 in the xenografts was observed after NK012 injection compared with CPT-11. NK012 showed significantly potent antitumor activity against an orthotopic glioblastoma multiforme xenograft and significantly longer survival rate than CPT-11 ($p = 0.0014$). This implies that NK012 can pass through the blood brain tumor barrier effectively. NK012, which combines enhanced distribution with prolonged sustained release, may be ideal for glioma treatment. Currently, a phase I study of NK012 is almost complete in Japan and the US. The present translational study warrants the clinical phase II study of NK012 in patients with malignant glioma.

Key words: glioma; drug delivery system; blood brain barrier (BBB); SN-38; micelles

Malignant astrocytomas, such as anaplastic astrocytoma and glioblastoma multiforme (GBM), are the most common and highly vascularized glial tumors of the brain. At least 80 percent of malignant gliomas are categorized as GBM.[1] Currently, GBM patients have a mean survival of only 50 weeks following the standard treatment consisting of surgical and adjuvant therapies.[2] A recent phase III randomized trial for newly diagnosed GBM demonstrated that radiation therapy with concurrent temozolomide treatment, followed by 6 months of temozolomide treatment was superior to radiation therapy alone in terms of overall survival.[3] In addition, several clinical trials have demonstrated that the median survival times of patients with recurrence were only 3–6 months.[4]

The anticancer plant alkaloid 7-ethyl-10-hydroxy-camptothecine (SN-38) is a broad spectrum anticancer agent targeting DNA topoisomerase I with a different mechanism of action compared with alkylating agents such as temozolomide. Although SN-38 has shown promising anticancer activity *in vitro* and *in vivo*, its clinical application has remained dormant because of its low therapeutic efficacy and severe toxic effects.[5,6] Irinotecan hydrochloride (CPT-11), a prodrug of SN-38, shows some antitumor activities in patient with recurrent GBM, with response rates of 0 to 17% in several trials.[7–10] CPT-11 activity is thus similar to that of other agents used for recurrent GBM.[9] A recent phase II trial for recurrent GBM demonstrated that the combination of CPT-11 and bevacizumab, an antivascular endothelial growth factor (VEGF) monoclonal antibody, is an effective treatment against the neoplasia with a 6-month progression-free survival rate of 46% and a 6-month overall survival rate of 77%.[11,12] However, there is an increased risk of developing venous thromboembolic disease and intracranial hemorrhage with this combination therapy. Therefore, there is an urgent need to develop treatment modalities by which cytotoxic drugs can exert more potent antitumor activity to their full potential with modest adverse effects and thereby reasonably prolong the overall survival in GBM patients.

The purpose of the drug delivery system (DDS) is to achieve selective delivery of antitumor agents to tumor tissue at an effective concentration for the appropriate duration of time in order to reduce the adverse effects of the administered drug and simultaneously enhance its antitumor effect. There are 2 main concepts in DDS, active targeting and passive targeting. Active targeting involves a monoclonal antibody and a ligand to a tumor-related receptor. Doxil, a doxorubicine incorporated polyethylene glycol conjugated liposome, is categorized under passive targeting agents and are already in clinical use.[13,14] NK012, a novel SN-38-incorporating polymeric micelle, is a prodrug of SN-38 similar to CPT-11 and categorized under passive targeting agent as well. Although CPT-11 is converted to SN-38 in tumors by carboxylesterase (CE), the metabolic conversion rate is within 2–8% of the original volume of CPT-11.[15,16] In contrast, the release rate of SN-38 from NK012 is 74% under physiologic pH condition even without CEs.[17] Recently, we have demonstrated that NK012 exerted significantly more potent antitumor activity against various human tumor xenografts than CPT-11.[17–20] However, there is a fundamental question whether such nanoparticles can reach brain tumors across the tumor microvessels. In the present study, therefore, we established an orthotopic glioma model in this experiment and then evaluated whether NK012 can pass through the BTB and exert its antitumor effect on orthotopic human glioma xenografts in comparison with CPT-11.

Material and methods

Drugs

NK012 and SN-38 were donated by Nippon Kayaku Co., Ltd. (Tokyo, Japan). The size of NK012 was ~20 nm in diameter with a narrow size distribution.[17] ACNU [1-(4-amino-2-methyl-5-pyrimidinyl) methyl-3-(2-chloroethyl)-3-nitrosourea, nimstine] was purchased from DAIICHI SANKYO Co., Ltd. (Tokyo, Japan). CDDP (cis-diamminedichloroplatinum) and CPT-11 were purchased from Yakult Co., Ltd. (Tokyo, Japan). Etoposide [4′demethlepipodophyllotoxin-9-(4, 6-O-ethylidene-β-D-glucopyranoside)] was purchased from BIOMOL (Plymouth Meeting, PA).

Grant sponsors: Ministry of Health, Labour and Welfare of Japan (Third Term Comprehensive Contorol Research for Cancer), Core Research for Evolutional Science and Technology, Ministry of Education, Culture, Sports, Science and Technology.

***Correspondence to:** Investigative Treatment Division, Research Center for Innovative Oncology, National Cancer Center Hospital East, 6-5-1 Kashiwanoha, Kashiwa 277-8577, Japan. Fax: +81-4-7134-6857.
E-mail: yhmatsum@east.ncc.go.jp.

Received 10 September 2008; Accepted after revision 28 October 2008
DOI 10.1002/ijc.24171
Published online 24 November 2008 in Wiley InterScience (www.interscience.wiley.com).

Cells and animals

Five human glioma cell lines, namely U87MG, U251MG, U118MG, LN18 and LN229, were obtained from the American Type Culture Collection (Rockville, MD). Cells were maintained in Dulbecco's modified Eagle's minimum essential medium supplemented with 10% fetal bovine serum (Cell Culture Technologies, Gaggenau-Hoerden, Germany), penicillin, streptomycin and amphotericin B (100 units/ml, 100 μg/ml and 25 μg/ml, respectively; Sigma, St. Louis, MO) in a humidified atmosphere containing 5% CO_2 at 37°C. Six- to eight-week-old athymic nude mice (nu/nu; Charles River Japan, Kanagawa, Japan) were used for this study. U87MG cells (1×10^5) were injected into the cerebral hemisphere using a Hamilton syringe through an entry point 1 mm anterior and 1.8 mm lateral to the bregma to an intraparenchymal depth of 2.5 mm. The rate of injection was 0.5 μl/min, and the needle was left in place for 5 min after completion of the injection. All animal procedures were performed in compliance with the Guidelines for the Care and Use of Experimental Animals established by the Committee for Animal Experimentation of the National Cancer Center, Japan; these guidelines meet the ethical standards required by law and also comply with the guidelines for the use of experimental animals in Japan.

Establishment of U87MG cell line stably expressing firefly luciferase and YFP mutant Venus

For the *in vivo* bioluminescence imaging of orthotopic brain tumors, the U87MG cell line stably expressing firefly luciferase and the YFP mutant Venus was established. Briefly, the coding sequence for firefly luciferase and Venus was subcloned into the the pIRES Vector (Clontech Laboratories, Mountain View, CA). The fragment consists of Luciferase-IRES-Venus generated from the plasmid with the restriction enzymes Nhe I and Not I. This fragment was subcloned into the pEF6/V5-His Vector (Invitrogen, Carlsbad, CA) to generate plasmids of pEF6-Lucifease IRES Venus. U87MG cells (2×10^6) were seeded onto 10-cm dishes 24 hr before transfection. The cells were transfected with 10 μg of pEF6-Lucifease IRES Venus using FuGENE HD Transfection Reagent (Roche Diagnostics, Mannheim, Germany) according to manufacturer's instructions, and then incubated for 48 hr at 37°C. The cells were then passaged in medium containing Blasticidin (10 μg/ml; InvivoGen, San Diego, CA) to select for the Blasticidin resistance gene integrated in the pEF6/V5-His plasmids. Venus expression was used as a surrogate marker of luciferase-positive cells. Venus-expressing U87MG cells (U87MG/Luc) were sorted using the BD FACS Aria cell sorter (BD Biosciences, San Jose, CA), and expanded in selection medium. The accuracy of a quantitive bioluminescence image as an indicator of U87MG/Luc cell number was analyzed using the Photon Imager animal imaging system *in vitro*, as described under *in vivo* growth inhibition assay. This analysis demonstrated clear correlation between a quantitive bioluminescence image and cell number ($R^2 = 0.99$). The sensitivity of U87MG/Luc cells to each drug (NK012, CPT-11, SN-38, ACNU, CDDP and etoposide) was almost similar to that of parental U87MG cells (data not shown).

In vitro *growth inhibition assay*

Cell growth inhibition was measured by the tetrazolium salt-based proliferation assay (WST assay; Wako Chemicals, Osaka, Japan). Briefly, cells (5×10^3 cells/well) in 96-well plates were incubated overnight. Then, growth medium was changed to new medium with various concentrations of SN-38, NK012, CPT-11, ACNU, etoposide and CDDP. After 72 hr of incubation, medium was changed to new medium containing 10% WST-8 reagents. After 1 hr of incubation, the absorbance of the formazan product formed was detected at 450 nm in a 96-well spectrophotometric plate reader (SpectraMax 190; Molecular Devices, Sunnyvale, CA). Cell viability was measured and compared with that of the control cells. Each experiment was carried out in triplicates and was repeated at least 3 times. Data were averaged and normalized against the nontreated controls to generate dose-response curves. The number of living cells (% Control) was calculated using the following formula: % Control = (each absorbance—absorbance of blank well)/absorbance of control well × 100.

Evaluation of NK012 and CPT-11 distribution in tumor tissue by fluorescence microscopy

The U87MG orthotopic xenograft model described earlier was used for the analysis of the biodistribution of NK012 and CPT-11. Twenty days after U87MG/Luc inoculation, the maximum tolerated dose (MTD) of NK012 (30 mg/kg) or CPT-11 (66.7 mg/kg) was injected intravenously into the tail vein of mice. At this point, tumor size reached to about 3 mm in diameter according to the preliminary experiment (data not shown). Two, 12 or 24 hr after NK012 or CPT-11 injection, mice were also administered with fluorescein *Lycopersicon esculentum* lectin (100 μl/mouse) (Vector Laboratories, Burlingame, CA) to visualize tumor blood vessels. Tumors were then excised and embedded in optimal cutting temperature compound and frozen at −80°C until use. Tissue sections (6 μm thick) were prepared using Tissue-Tek Cryo3 (Sakura Finetek USA, Inc., Torrance, CA), and frozen sections were examined under a fluorescence microscope, BIOREVO BZ9000 (Keyence, Osaka, Japan), at an excitation wavelength of 377 nm and an emission wavelength 447 nm to evaluate the distribution of CPT-11 and NK012 within the tumor tissues. Because formulations containing SN-38 bound *via* ester bonds possess a particular fluorescence, both CPT-11 and NK012 were detected under the same fluorescence conditions. Image data were recorded using BZ-II Analyzer 1.10 software (Keyence, Osaka, Japan).

Pharmacokinetics study of NK012 and CPT-11

Female BALB/c nude mice bearing U87MG/Luc tumor ($n = 3$) were used for the analysis of the biodistribution of NK012 and CPT-11. Twenty days after the intracranial injection of U87MG/Luc cells, NK012 (30 mg/kg) or CPT-11 (66.7 mg/kg) was intravenously administered to the mice. Under anesthesia, blood, normal brain tissues and tumor tissues were obtained 2, 12, 24 and 72 hr after NK012 or CPT-11 administration. Blood samples were collected in microtubes and immediately centrifuged at 1,600*g* for 15 min at 4°C. All samples were stored at −80°C until use.

The normal brain and tumor samples were rinsed with physiologic 0.9% NaCl solution, mixed with 0.1 M glycine-HCl buffer (pH 3.0)/methanol at 5 w/w%, and then homogenized. To analyze the concentration of free SN-38 and CPT-11, 100 μl of the tumor homogenates was mixed with 20 μl of 1 mM phosphoric acid/methanol (1:1), 40 μl of ultrapure water and 60 μl of camptothecin solution (10 ng/ml for SN-38 and 15 ng/ml for CPT-11) as an internal standard. To quantify free SN-38 and CPT-11 in plasma, 25 μl of plasma was mixed with 25 μl of 0.1 M HCl, and then added with 20 μl of 1 mM phosphoric acid/methanol (1:1) and 100 μl of CPT solution (10 ng/ml both for SN-38 and CPT-11). The samples were vortexed vigorously for 10 sec, and then filtered through Ultrafree-MC centrifugal filter devices with a cut-off molecular diameter of 0.45 μm (Millipore Co., Bedford, MA). Reversed-phase HPLC was performed at 35°C on a Mightysil RP-18 GP column 150 × 4.6 mm^2 (Kanto Chemical Co., Inc., Tokyo, Japan). Fifty microliters of a sample was injected into an Alliance Waters 2795 HPLC system (Waters, Milford, MA) equipped with a Waters 2475 multi λ fluorescence detector. Fluorescence originating from SN-38 was detected at 540 nm with an excitation wavelength of 365 nm and that originating from CPT-11 was detected at 430 nm with an excitation wavelength of 365 nm. The mobile phase was a mixture of 100 nmol/l ammonium acetate (pH 4.2) and methanol (11:9 (v/v)). The flow rate was 1.0 ml/min. The content of SN-38 was calculated by measuring the relevant peak area and calibrating against the corresponding peak area derived from the CPT internal standard. Peak data were recorded using a chromatography management system (MassLynx v4.0, Waters).

For polymer-bound SN-38 detection, SN-38 was released from the conjugate. Briefly, 20 μl of plasma and 100 μl of tissue